An adaptive finite element/meshless coupled method based on local maximum entropy shape functions for linear and nonlinear problems

Z. Ullah, W. M. Coombs, C. E. Augarde[1]

School of Engineering and Computing Sciences, Durham University, Durham, DH1 3LE, UK

Abstract

In this paper, an automatic adaptive coupling procedure is proposed for the finite element method (FEM) and the element-free Galerkin method (EFGM) for linear elasticity and for problems with both material and geometrical nonlinearities. In this new procedure, initially the whole of the problem domain is modelled using the FEM. During an analysis, those finite elements which violate a predefined error measure are automatically converted to an EFG zone. This EFG zone can be further refined by adding nodes, thus avoiding computationally expensive FE remeshing. Local maximum entropy shape functions are used in the EFG zone of the problem domain for two reasons: their weak Kronecker delta property at the boundaries allows straightforward imposition of essential boundary conditions and also provides a natural way to couple the EFG and FE regions compared to the use of moving least squares basis functions. The Zienkiewicz & Zhu error estimation procedure with the superconvergent patch method for strains and stresses recovery is used in the FE region of the problem domain, while the Chung & Belytschko error estimation procedure is used in the EFG region.

Keywords:
Meshless method, Maximum entropy shape functions, FE-EFGM coupling, Error estimation, Adaptivity, Superconvergent patch recovery

[1]Correspondence to: C.E. Augarde, School of Engineering and Computing Sciences, Durham University, Durham, DH1 3LE, UK. E-mail: charles.augarde@dur.ac.uk

1. Introduction

Meshless methods remain of interest in the computational mechanics community, in particular the element-free Galerkin method (EFGM) [1], because in these methods only a set of nodes is required for the problem discretisation, making them ideal for modelling problems with large deformation, material damage, projectile penetration, fragmentation, crack growth and moving boundaries, the details of which can be found in [2, 3, 4, 5, 6, 7, 8, 9, 10, 11, 12]. However it is well-known that they tend to be more computationally expensive than finite element methods (FEMs) set the same job. It makes sense therefore to look at coupled modelling, where meshless discretisation is used in regions of a domain which most benefit from their greater accuracy and lack of a mesh, while maintaining a finite element discretisation elsewhere in the domain. In most of the coupling procedures proposed to date it is necessary to specify FE and EFG regions in the problem domain at the start of simulation, in the preprocessing stage. These regions are fixed in the problem domain, and performance is then highly user dependent. For practical engineering problems, it will be very difficult, especially for an inexperienced user, to decide on appropriate FE and EFG regions in a given problem domain. For problems with both geometric and material nonlinearities, this problem is even more intractable, as geometry is changing during the simulation. To overcome these problems, an automatic adaptive FE-EFGM coupled method is proposed in this paper for linear and nonlinear problems where initially the whole of the problem domain is modelled using the FEM. During an analysis those finite elements which violate a predefined error measure are automatically converted to an EFG zone. This zone can be further refined by adding nodes, thus achieving adaptivity without any (computationally expensive) FE remeshing.

Proper FE-EFGM coupling is an important issue in the development of meshless methods, and different coupling strategies are available in the literature. The most prominent at present is probably that proposed in [13], in which interface/transition elements are used between the FE and the EFG regions of the problem domain. In that procedure moving least squares (MLS) shape functions are used in the EFG region of the problem domain, while hybrid shape functions, combining both MLS and FE shape functions, are used in the interface region. Other commonly used methods for FE-EFGM coupling are the continuous blending method in [14, 15], methods based on Lagrange multipliers [16, 17], on transition or bridge regions [18]

and methods based on a collocation approach [19]. A comprehensive review of different FE-EFGM coupling procedures up to 2005 can be found in [20]. A new coupling procedure for FE-EFGM has recently been proposed by the authors in [21] for linear elastic and geometrically nonlinear problems. In this coupling procedure, max-ent shape functions are used in the EFG region of the problem domain. Their weak Kronecker delta property allows imposition of the essential boundary conditions directly and a direct coupling of the FE and the EFG regions without transition/interface elements or any of the other special techniques used previously. In this paper we extend this work into an adaptive framework as well as into materially nonlinear problems. Only a very limited literature is available for *adaptive* FE-meshless coupling, for instance references [22, 23] deal only with two-dimensional problems without proper error estimation and with no further adaptivity in the meshless zone.

The method presented here uses a total Lagrangian formulation for modelling finite deformation due to its computational efficiency, and performance with material nonlinearity is demonstrated using the Prandtl-Reuss constitutive model (the von Mises yield function with perfect plasticity and associated flow) although any similar constitutive model could be used. For linear elastic problems, the well-established error estimation procedure of Zienkiewicz & Zhu [24] with the superconvergent convergent patch recovery (SPR) method for recovery of the nodal stresses [25, 26] is used in the FE region to determine the elements requiring conversion to EFG regions. The Chung & Belytschko [27] error estimator is used in the EFG region for further adaptive refinement. For nonlinear problems, incremental forms of the Zienkiewicz & Zhu error estimator [28] and the Chung & Belytschko error estimator [29] are used. Full details of each component are given below, organized as follows. The theoretical background and detailed formulation of the max-ent shape functions are presented in §2. These shape functions are then used in the EFGM, for which the modified formulations are given in §3. The details of the coupling between the FE and EFG region based on max-ent shape function are given in §4. The adaptive FE-EFGM coupling procedure for linear elastic and nonlinear problems is described in §5, including error estimation procedure for both FEM and EFGM in §5.1. The corresponding refinement strategy is then given in §5.2 and the full adaptively coupled FE-EFGM algorithm is described in §5.3. Numerical examples are given in §6 to show the implementation and performance of the proposed adaptive FE-EFGM method. Concluding remarks follow in §7.

2. Maximum entropy shape functions

Max-ent shape functions, based on the idea of informational entropy [30, 31] and the principle of max-ent [32, 33], were introduced in [34] to formulate interpolants for polygons. These shape functions are not however suitable to be directly used for meshless methods as they extend to the global problem domain. More useful shape functions termed as "local", which can be defined for a set of nodes, were first introduced in [35] , where their weak Kronecker delta property was also highlighted. Compact support shape functions were then derived using Gaussian weight functions (or priors) in [35], work which was extended in [36] to any weight function (or generalized prior). First-order consistent max-ent shape functions [36] were then extended to second order in [37] and higher order in [38] and max-ent was used in [39] for the automatic calculation of the nodal domain of influence within a meshless method.

The max-ent concept comes from information theory [31] where a measure of the amount of information or uncertainty of a finite scheme is termed information entropy and is given as

$$H(p_1, ..., p_n) = -\sum_{i=1}^{n} p_i \log p_i, \tag{1}$$

where $p_1, ..., p_n$ are probabilities of n mutually independent events. The most likely probability distribution is obtained by using Jaynes' principle of max-ent [33], i.e. maximising (1) subject to constraints $\sum_{i=1}^{n} p_i = 1$ and $\sum_{i=1}^{n} p_i g_r(x_i) = \langle g_r(x) \rangle$, where $\langle g_r(x) \rangle$ is the expectation of a function $g_r(x)$. The max-ent approach can be used to derive shape functions by seeing an analogy between the probabilities above and the shape function values themselves. A useful local shape function formulation can be obtained [36] by incorporating prior distributions w_i which can be regarded as weight functions that provide compact or local support, and then maximising the following

$$H(\phi, w) = -\sum_{i=1}^{n} \phi_i \log \left(\frac{\phi_i}{w_i} \right), \tag{2}$$

subject to the standard constant and linearly reproducing constraints

$$\sum_{i=1}^{n}\phi_i{=}1, \qquad \sum_{i=1}^{n}\phi_i x_i = x, \qquad \sum_{i=1}^{n}\phi_i y_i = y \qquad \text{and} \qquad \sum_{i=1}^{n}\phi_i z_i = z. \tag{3}$$

Shape functions can be derived as

$$\phi_i = \frac{Z_i}{Z} \tag{4}$$

where

$$Z_i = w_i e^{-\lambda_1\widetilde{x}_i-\lambda_2\widetilde{y}_i-\lambda_3\widetilde{z}_i} \qquad \text{and} \qquad Z = \sum_{j=1}^{n} Z_j, \tag{5}$$

in which w_i is the weight function associated with node i, evaluated at point $\mathbf{x} = (x, y)^T$, $\widetilde{x}_i = x_i - x$, $\widetilde{y}_i = y_i - y$ and $\widetilde{z}_i = z_i - z$ are shifted coordinates. n is the number of nodes in support at $\mathbf{x}$ and λ_1, λ_2 and λ_3 are Lagrange multipliers which can be found from

$$(\lambda_1, \lambda_2, \lambda_3) = \text{argmin} F(\lambda_1, \lambda_2, \lambda_3) \qquad \text{where} \qquad F(\lambda_1, \lambda_2, \lambda_3) = \log(Z). \tag{6}$$

F is a convex function and Newton's method is used to solve (6) to find the Lagrange multipliers which can then be used in the expressions for the shape functions. The shape function derivatives follow as [40]

$$\nabla\phi_i = \phi_i\left(\nabla f_i - \sum_{i=1}^{n}\phi_i\nabla f_i\right), \tag{7}$$

where

$$\nabla f_i = \frac{\nabla w_i}{w_i} + \boldsymbol{\lambda} + \widetilde{\mathbf{x}}_i\left[H^{-1} - H^{-1}A\right] \qquad \text{and} \qquad A = \sum_{k=1}^{n}\phi_k\widetilde{\mathbf{x}}_k \otimes \frac{\nabla w_k}{w_k}. \tag{8}$$

Where H is the Hessian matrix and the dyadic product $\otimes$ of two vector $\mathbf{a}$ and $\mathbf{b}$ is a second order tensor, i.e. $\mathbf{a}\otimes\mathbf{b}$ defined as $\mathbf{a}\otimes\mathbf{b} = \mathbf{a}\mathbf{b}^T$.

3. Element-free Galerkin method

The element-free Galerkin method was proposed in [1], based on a global weak form. It is one of the most commonly used meshless methods and is

based on the earlier diffuse element method [41]. In the EFGM, moving least squares (MLS) shape functions are used for the approximation of the field variables, background integration cells are used for numerical integration and Lagrange multipliers are used for the imposition of essential boundary conditions.

Three-dimensional formulations are given here for the EFGM with maxent shape functions, but it is straightforward to modify for one- and two-dimensional cases. Consider a three-dimensional problem defined in the domain Ω and bounded by Γ. The equilibrium equations at a point $\mathbf{x}$ are written as

$$\boldsymbol{\nabla}^T \boldsymbol{\sigma} + \mathbf{b}_f = \mathbf{0} \qquad \text{in } \Omega, \tag{9}$$

where $\boldsymbol{\sigma} = \left\{ \begin{array}{cccccc} \sigma_{xx} & \sigma_{yy} & \sigma_{zz} & \sigma_{xy} & \sigma_{yz} & \sigma_{xz} \end{array} \right\}^T$ is the Cauchy stress vector, $\mathbf{b}_f = \left\{ \begin{array}{ccc} b_{f_x} & b_{f_y} & b_{f_z} \end{array} \right\}^T$ is the body force vector, where b_{f_x}, b_{f_y} and b_{f_z} are the body forces in x, y and z directions respectively and $\boldsymbol{\nabla}$ is the differential operator and is written as $\boldsymbol{\nabla} = \begin{bmatrix} \dfrac{\partial}{\partial x} & 0 & 0 \\ 0 & \dfrac{\partial}{\partial y} & 0 \\ 0 & 0 & \dfrac{\partial}{\partial z} \\ \dfrac{\partial}{\partial y} & \dfrac{\partial}{\partial x} & 0 \\ 0 & \dfrac{\partial}{\partial z} & \dfrac{\partial}{\partial y} \\ \dfrac{\partial}{\partial z} & 0 & \dfrac{\partial}{\partial x} \end{bmatrix}$.

The boundary conditions associated with (9) are

$$\mathbf{u} = \bar{\mathbf{u}} \qquad \text{on } \Gamma_u, \tag{10a}$$

$$\boldsymbol{\sigma}\mathbf{n} = \bar{\boldsymbol{t}} \qquad \text{on } \Gamma_t, \tag{10b}$$

where (10a) is essential or Dirichlet boundary condition and (10b) is natural or Neumann boundary condition. Here $\mathbf{u} = \left\{ \begin{array}{ccc} u_x & u_y & u_z \end{array} \right\}^T$ is the displacement vector, where u_x, u_y and u_z are the displacements in x, y and z directions, and $\mathbf{n} = \left\{ \begin{array}{ccc} n_x & n_y & n_z \end{array} \right\}^T$ is the outward unit normal to the boundary Γ, $\bar{\boldsymbol{t}}$ is the prescribed traction on the traction boundary, Γ_t, and $\bar{\mathbf{u}}$ is the prescribed displacement on the essential boundaries, Γ_u. Due to the

use of MLS shape functions, which do not posses the Kronecker delta property, constrained Galerkin weak form with Lagrange multipliers are used in [1] but due to the use of max-ent shape functions Galerkin weak form is used directly, which is written as

$$\int_{\Omega} \delta \left(\nabla \mathbf{u}\right)^T \mathbf{D} \left(\nabla \mathbf{u}\right) \mathrm{d}\Omega - \int_{\Omega} \delta \mathbf{u}^T \mathbf{b}_f \mathrm{d}\Omega - \int_{\Gamma_t} \delta \mathbf{u}^T \bar{\mathbf{t}} \mathrm{d}\Gamma = 0, \tag{11}$$

where $\mathbf{D}$ is the material stiffness matrix. After discretising the problem with a set of nodes, displacement at a point of interest $\mathbf{x}$ is written as

$$\mathbf{u}^h \left(\mathbf{x}\right) = \left\{ \begin{array}{c} u_x \\ u_y \\ u_z \end{array} \right\} = \sum_{i=1}^{n} \left[\begin{array}{ccc} \phi_i & 0 & 0 \\ 0 & \phi_i & 0 \\ 0 & 0 & \phi_i \end{array} \right] \left\{ \begin{array}{c} u_{xi} \\ u_{yi} \\ u_{zi} \end{array} \right\} = \sum_{i=1}^{n} \boldsymbol{\phi}_i \mathbf{u}_i, \tag{12}$$

where $\mathbf{u}^h \left(\mathbf{x}\right)$ is an approximation of the displacements at a point $\mathbf{x}$, n is the number of nodes in the support of point $\mathbf{x}$, $\boldsymbol{\phi}_i$ is a matrix of the max-ent shape functions for node i at a point $\mathbf{x}$ and $\mathbf{u}_i$ are known as fictitious nodal values or nodal parameters. Using (12) in (11) and after simplification, the final discrete system of linear equation is written as

$$\mathbf{K}\mathbf{u} = \mathbf{f}, \tag{13}$$

where

$$\mathbf{K}_{ij} = \int_{\Omega} \mathbf{B}_i^T \mathbf{D} \mathbf{B}_j \mathrm{d}\Omega, \tag{14}$$

$$\mathbf{f}_i = \int_{\Gamma_t} \boldsymbol{\phi}_i \bar{\boldsymbol{t}} \mathrm{d}\Gamma + \int_{\Omega} \boldsymbol{\phi}_i \mathbf{b}_f \mathrm{d}\Omega, \tag{15}$$

$$\mathbf{B}_i = \begin{bmatrix} \dfrac{\partial \phi_i}{\partial x} & 0 & 0 \\ 0 & \dfrac{\partial \phi_i}{\partial y} & 0 \\ 0 & 0 & \dfrac{\partial \phi_i}{\partial z} \\ \dfrac{\partial \phi_i}{\partial y} & \dfrac{\partial \phi_i}{\partial x} & 0 \\ \dfrac{\partial \phi_i}{\partial z} & 0 & \dfrac{\partial \phi_i}{\partial x} \\ 0 & \dfrac{\partial \phi_i}{\partial z} & \dfrac{\partial \phi_i}{\partial y} \end{bmatrix}, \tag{16}$$

and

$$\mathbf{D} = \frac{E}{(1+\nu)(1-2\nu)} \begin{bmatrix} 1-\nu & \nu & \nu & 0 & 0 & 0 \\ \nu & 1-\nu & \nu & 0 & 0 & 0 \\ \nu & \nu & 1-\nu & 0 & 0 & 0 \\ 0 & 0 & 0 & \dfrac{1-2\nu}{2} & 0 & 0 \\ 0 & 0 & 0 & 0 & \dfrac{1-2\nu}{2} & 0 \\ 0 & 0 & 0 & 0 & 0 & \dfrac{1-2\nu}{2} \end{bmatrix}. \tag{17}$$

where ν is the Poisson's ratio and E is the modulus of elasticity. To perform the integrations in (14) and (15) numerically, the problem domain Ω and traction boundary Γ_t are divided into a number of non-overlapping background cells.

In the case of nonlinear problems, a total Lagrangian formulation is used here to model finite deformation, in which all the kinematical variables are referred back to the original or undeformed configuration and for modelling elasto-plasticity, the Prandtl-Reuss constitutive model is used. Here the deformation gradient is used, which is the fundamental measure of deformation, providing the relationship between the current and reference configurations, that is

$$\mathbf{F} = \frac{\partial \mathbf{x}}{\partial \mathbf{X}}, \tag{18}$$

where $\mathbf{x}$ and $\mathbf{X}$ are the coordinates of a point in the current and reference

configurations respectively. The work-conjugate stress and strain measures used in this paper are logarithmic strain $\boldsymbol{\varepsilon}$ and Kirchhoff stress $\boldsymbol{\tau}$ [42], which are given as [43]

$$\boldsymbol{\varepsilon} = \frac{1}{2} \ln \mathbf{b}, \qquad \boldsymbol{\tau} = J\boldsymbol{\sigma}, \tag{19}$$

where $\boldsymbol{\sigma}$ is the Cauchy stress, $\mathbf{b}$ is the left Cauchy-Green tensor and J is the determinant of the deformation gradient $\mathbf{F}$. In total Lagrangian formulations, there is no need to update the geometry, the shape functions and the corresponding derivatives are calculated and stored at the start of the simulation and are used in every solution step in each Newton-Raphson iteration. In this case, the deformation gradient $\mathbf{F}_{n+1}$ for increment $n+1$ is calculated from the total nodal parameters or fictitious nodal values $\mathbf{u}_i$ and the increment in the deformation gradient $\Delta\mathbf{F}$ is then be calculated using the deformation gradient $\mathbf{F}_n$ of the previous converged iteration, i.e.

$$\Delta\mathbf{F} = \mathbf{F}_{n+1}\,\mathbf{F}_n^{-1}, \qquad \mathbf{F}_{n+1} = \mathbf{I} + \sum_{i=1}^{n} \mathbf{u}_i \begin{bmatrix} \dfrac{\partial \phi}{\partial X} \\ \dfrac{\partial \phi}{\partial Y} \\ \dfrac{\partial \phi}{\partial Z} \end{bmatrix}_i^T, \tag{20}$$

where $\mathbf{I}$ is a 3×3 identity matrix, n is the number of nodes in support and the shape function derivatives are calculated with reference to the original geometry. The trial elastic left Cauchy-Green strain matrix $\mathbf{b}^e_{tr}$ is written as

$$\mathbf{b}^e_{tr} = \Delta\mathbf{F}\,\mathbf{b}^e_n\,\Delta\mathbf{F}^T, \tag{21}$$

where $\mathbf{b}^e_n$ is the value of the elastic left Cauchy-Green strain matrix at the end of previous increment and is obtained by rearranging (19) in terms of $\mathbf{b}$ and using $\boldsymbol{\varepsilon} = \boldsymbol{\varepsilon}^e_n$, where $\boldsymbol{\varepsilon}^e_n$ is the elastic strain from the previously converged load step. (21) can be used in (19) to calculate the trial elastic strain $\boldsymbol{\varepsilon}^e_{tr}$, which is input to the constitutive model, the output of which includes elastic strain $\boldsymbol{\varepsilon}^e$, stress $\boldsymbol{\sigma}$ and consistent or algorithmic tangent D^{alg}. A Newton-Raphson incremental-iterative procedure is used, i.e. load is applied incrementally in steps and convergence is sought for each increment, using

$$\mathbf{f}^{int}_{n+1}\left(\mathbf{u}_{n+1}\right) - \mathbf{f}^{ext}_{n+1} = \mathbf{oobf}_{n+1} = \mathbf{0}, \tag{22}$$

where $n+1$ is the global Newton-Raphson iteration counter, $\mathbf{f}_{n+1}^{int}$ and $\mathbf{f}_{n+1}^{ext}$ are the global internal and external force vectors respectively, $\mathbf{oobf}_{n+1}$ is the residual or out-of-balance force and $\mathbf{u}_{n+1}$ is a vector of nodal parameters or fictitious nodal values. The expression for the internal forces for an increment $n+1$ are given as

$$\mathbf{f}_{n+1}^{int} = \int_{\Omega} \mathbf{G}^T \mathbf{P} \mathrm{d}\Omega = \sum_{i=1}^{n_g} \mathbf{G}_i^T \mathbf{P}_i \left|\mathbf{J}_i\right| w_i, \tag{23}$$

where n_g are the total number of Gauss points in the problem domain, $\mathbf{J}_i$ and w_i are the Jacobian and weights associated with each Gauss points respectively, $\mathbf{G}$ is the 9-component strain-displacement matrix, consisting of the shape function derivatives with respect to the original configuration and is written as

$$\mathbf{G}_i = \begin{bmatrix} \dfrac{\partial \phi_i}{\partial X} & 0 & 0 \\ 0 & \dfrac{\partial \phi_i}{\partial Y} & 0 \\ 0 & 0 & \dfrac{\partial \phi_i}{\partial Z} \\ \dfrac{\partial \phi_i}{\partial Y} & 0 & 0 \\ 0 & \dfrac{\partial \phi_i}{\partial X} & 0 \\ 0 & \dfrac{\partial \phi_i}{\partial Z} & 0 \\ 0 & 0 & \dfrac{\partial \phi_i}{\partial Y} \\ 0 & 0 & \dfrac{\partial \phi_i}{\partial X} \\ \dfrac{\partial \phi_i}{\partial Z} & 0 & 0 \end{bmatrix} \tag{24}$$

and $\mathbf{P}$ is the nine component non-symmetric first Piola-Kirchhoff stress and is given as

$$\mathbf{P} = J\boldsymbol{\sigma}\mathbf{F}^{-T} = \boldsymbol{\tau}\mathbf{F}^{-T}. \tag{25}$$

The equation for the global stiffness matrix in this case is written as

$$\mathbf{K} = \int_{\Omega} \mathbf{G}^T \widetilde{\mathbf{A}} \mathbf{G} \mathrm{d}\Omega, \tag{26}$$

where $\widetilde{\mathbf{A}}$ is the isotropic material stiffness tangent and is written as

$$\widetilde{\mathbf{A}} = \frac{\partial \mathbf{P}}{\partial \mathbf{F}} = \frac{\partial \boldsymbol{\tau} \mathbf{F}^{-T}}{\partial \mathbf{F}}, \tag{27}$$

The partial derivative is expressed as (index notation is used here for better presentation)

$$\widetilde{A}_{ijkl} = \frac{\partial \tau_{ip} F^{-1}_{jp}}{\partial F_{kl}} = \frac{\partial \tau_{ip}}{\partial F_{kl}} F^{-1}_{jp} - P_{ik} F^{-1}_{jk}. \tag{28}$$

After using the chain rule, the partial derivative $\frac{\partial \tau_{ip}}{\partial F_{kl}}$ is written as

$$\frac{\partial \tau_{ip}}{\partial F_{kl}} = \frac{\partial \tau_{ip}}{\partial \left(\varepsilon^e_t\right)_{ab}} \frac{\partial \left(\varepsilon^e_t\right)_{ab}}{\partial \left(b^e_t\right)_{cd}} \frac{\partial \left(b^e_t\right)_{cd}}{\partial F_{kl}}, \tag{29}$$

where $\frac{\partial \tau_{ip}}{\partial \left(\varepsilon^e_t\right)_{ab}} = D^{alg}_{ipab}$ is infinitesimal consistent or algorithmic tangent and $\frac{\partial \left(\varepsilon^e_t\right)_{ab}}{\partial \left(b^e_t\right)_{cd}} = L_{abcd}$ is the the partial derivative of logarithm of b^e_t with respect to its components and is written as

$$\frac{\partial \left(b^e_t\right)_{cd}}{\partial F_{kl}} = \delta_{ck} \left(\left(F^{-1}_n\right)_{lw} \left(b^e_n\right)_{wv} \Delta F_{dv} \right) + \delta_{ck} \left(\Delta F_{cw} \left(b^e_n\right)_{wv} \left(F^{-1}_n\right)_{lv} \right). \tag{30}$$

Effective plastic strain is used as one of the measures to evaluate the performance of the proposed model and is given as

$$\overline{\boldsymbol{\varepsilon}^p} = \sqrt{\frac{2}{3} \left(\boldsymbol{\varepsilon}^p\right)^T \left(\boldsymbol{\varepsilon}^p\right)}, \tag{31}$$

where $\boldsymbol{\varepsilon}^p$ is plastic strain.

4. FE-EFGM Coupling using max-ent shape functions

In the FE-EFGM coupling based on the interface elements [13], MLS shape functions are used in the EFG zone for the approximation of the field

variables. The MLS shape functions do not possess the Kronecker delta property like the FE shape functions and due to this reason interface elements are introduced between the FE and the EFG zones [13], to properly couple the two regions. The shape functions for the interface elements are hybrid shape functions of the FE and the EFG shape functions to make the displacement continuous across the FE-EFGM interface. The details of the FE-EFGM coupling based on the interface elements is not given here and can be found in the relevant literature. In this paper, max-ent shape functions are used in the EFG region of the problem domain, which provide a natural way to couple the FEM and the EFGM without using interface elements or transition regions between the FE and EFG zones because of their weak Kronecker delta property at the boundaries. A sample mixed FE and EFG discretization is shown in Figure 1, where Ω_E and Ω_F are the EFG and the FE regions and Γ is the boundary between these two regions. The nodes on the boundary Γ between the EFG and FE regions, shown in green in Figure 1, are used in the displacement approximation for both the EFG and the FE regions. Displacement can be approximated at point $\mathbf{x}$ in a similar way in the two

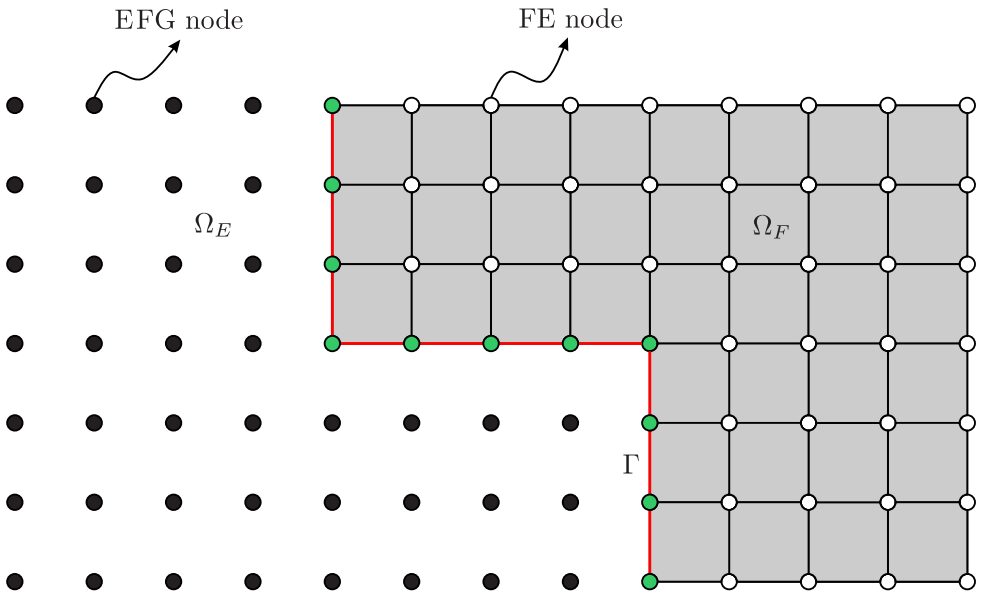

Figure 1: FE-EFGM coupling using max-ent shape functions

regions, i.e.

$$u^h(\mathbf{x}) = \sum_{i=1}^{n} \widetilde{N}_i(\mathbf{x})\, u_i, \tag{32}$$

where $u^h(\mathbf{x})$ is the approximate displacement component at point $\mathbf{x}$, $\widetilde{N}_i(\mathbf{x})$ is either the FE or the EFG shape function for node i evaluated at point $\mathbf{x}$, n is the number of nodes in support of point $\mathbf{x}$ and u_i are either nodal displacements in the case of the FEM, or nodal parameters in case of the EFGM.

5. Adaptive FE-EFGM

All analyses using this method start with a domain discretised entirely with finite elements. An error estimator is used to flag elements which require conversion to EFG zones. The refinement strategy then comprises changing the nodes on these elements to become EFG nodes, and the original finite element regions become the integration cells for the EFGM. By this process the method uses the finite element grid to form the integration cells and avoids generating a separate cell layout. Refinement is not confined to this conversion from FE to EFG: further refinement of EFG regions is also included.

5.1. Error estimation

The Zienkiewicz & Zhu [25] error estimator with the SPR method for recovery of stresses and strain are used in the FE region of the problem domain, while the Chung & Belytschko [27] error estimation is used in the EFG region of the problem domain. The basic idea of both of these error estimation procedures are to use the difference between projected and the direct numerical solutions and are similar to the conventional recovery type error estimation method in the FEM [26]. Despite the calculation of nodal stresses and strains, the error estimation procedures for the FE and EFG regions work similarly, i.e. in FE and EFG regions the procedure goes element-wise and background cells-wise respectively.

The exact error in stress or strain fields at a point $\mathbf{x}$ is the difference between the exact and numerical values, i.e.

$$\boldsymbol{\sigma}^e(\mathbf{x}) = \boldsymbol{\sigma}(\mathbf{x}) - \boldsymbol{\sigma}^h(\mathbf{x}) \qquad \text{and} \qquad \boldsymbol{\varepsilon}^e(\mathbf{x}) = \boldsymbol{\varepsilon}(\mathbf{x}) - \boldsymbol{\varepsilon}^h(\mathbf{x}), \tag{33}$$

where $\boldsymbol{\sigma}^e(\mathbf{x})$ and $\boldsymbol{\varepsilon}^e(\mathbf{x})$ are the exact error in the stress and strain at a point $\mathbf{x}$ respectively, $\boldsymbol{\sigma}(\mathbf{x})$ and $\boldsymbol{\varepsilon}(\mathbf{x})$ are the exact stress and strain at a point $\mathbf{x}$ while $\boldsymbol{\sigma}^h(\mathbf{x})$ and $\boldsymbol{\varepsilon}^h(\mathbf{x})$ are the numerical stress and strain at a point $\mathbf{x}$. The error for the individual cell and for the whole domain can then be found using an appropriate norm; error in energy norm is used in this paper. In this case, the exact local error in energy norm $\|e_e\|$ and the corresponding exact local energy norm $\|U_e\|$ for either an individual FE or EFG background cell Ω_e are given by

$$\|e_e\| = \left(\int_{\Omega_e} \left(\boldsymbol{\sigma}^e(\mathbf{x})\right)^T \mathbf{D}^{-1} \left(\boldsymbol{\sigma}^e(\mathbf{x})\right) \mathrm{d}\Omega_e \right)^{\frac{1}{2}}$$

$$\text{and} \qquad \|U_e\| = \left(\int_{\Omega_e} \left(\boldsymbol{\sigma}(\mathbf{x})\right)^T \mathbf{D}^{-1} \left(\boldsymbol{\sigma}(\mathbf{x})\right) \mathrm{d}\Omega_e \right)^{\frac{1}{2}}, \quad (34)$$

where subscript e shows an individual FE or EFG background cell with domain Ω_e. As the exact stresses and strains are not available for real-life problems, so the projected stress $\boldsymbol{\sigma}^p(\mathbf{x})$ and projected strain $\boldsymbol{\varepsilon}^p(\mathbf{x})$ are used in (33) and (34) instead of the exact stress and exact strain respectively and the calculated error in energy norm $\|e_e^p\|$ is then know as the estimated error in energy norm. Equations for the global error in energy norm and the corresponding global energy norm for the problem domain Ω are then written as

$$\|e^p\|^2 = \sum_{i=1}^{n_e} \|e_e^p\|_i^2 \qquad \text{and} \qquad \|U\|^2 = \sum_{i=1}^{n_e} \|U_e\|_i^2, \quad (35)$$

where for linear elastic problems n_e is the number of FEs in the first iteration and the number of EFG background cells in the consecutive iterations. Global relative percentage error η and permissible local error in an individual FE or EFG background cells $\overline{\|e_e\|}$ are then written as

$$\eta = \frac{\|e^p\|}{\|U\|} \times 100 \qquad \text{and} \qquad \overline{\|e_e\|} = \frac{\overline{\eta}}{100} \left(\frac{\|U\|^2}{n_e} \right)^{\frac{1}{2}}, \quad (36)$$

where $\overline{\eta}$ is the global permissible relative error for the whole problem domain.

The adaptive procedure is triggered by the global relative error, i.e. when $\eta > \overline{\eta}$ and the conversion of FEs to EFG background cells or further refinement of EFG background cells is performed when $\frac{\left\|e_e^p\right\|}{\|e_e\|} > 1$.

Recovery type error estimation procedures have already been used by other researchers in the literature for nonlinear problems in adaptive analysis. The Zienkiewicz & Zhu error estimation procedure was extended to nonlinear problems for the first time in [28] and was used for two-dimensional problems subjected to small strain elasto-plasticity, in which for each solution step, incremental error in energy norm was calculated from nodal stresses and nodal incremental strains recovered using the recovery by equilibrium in patches [44] and SPR method respectively. Further applications of the Zienkiewicz & Zhu error estimation procedure in two-dimensional nonlinear problems can be found in a number of references, e.g. in [45], the SPR method was used to estimate error for two-dimensional footings on soil problems, subjected to large deformation with elasto-plasticity. 6-node triangular elements with three Gauss points per element were used to discretise the problems and the L_2 norm of error in strain was used for the adaptive analysis. In [46], recovery of the Cauchy stress was performed by the SPR method for two-dimensional problems with large deformation using hyperelasticity as a material model. The improved SPR method was introduced for two-dimensional large deformation problems in [47], in which integration points were used as sampling points and bilinear 4-node quadrilateral elements with (2×2) Gauss points were used in the analysis. It was shown in [48, 49] that the SPR method can perform well, even if the sampling points used for stress recovery are not the superconvergent points. This information is very helpful to extend the SPR method originally proposed for linear problems to nonlinear problems, where most of the path dependent variables are available at the integration points, which are generally not superconvergent. The use of integration points as sampling points also allows the inclusion of more terms in the polynomial of the least squares fitting over the patch of elements, which is normally impossible with the superconvergent points, because they are few in number. The nonexistence of superconvergent points in the case of nonlinear problems was also mentioned in [46], where it was concluded that using (2×2) integration points in linear 4-node quadrilateral elements as sampling points led to better performance than using one superconvergent Gauss point. Gauss points were also used as sampling points in [47] for problems subjected to large deformation.

The Zienkiewicz & Zhu error estimation procedure with the SPR method for stress recovery has been used in a number of linear and nonlinear three-dimensional problems. In [50], the SPR method was used to calculate error in three-dimensional h-adaptive analysis for linear-elastic problems. Adaptive FEA based on the modified SPR method was used to model curved cracks in three-dimensional problems in [51]. In [52], the SPR method was used for error estimation in three-dimensional nonlinear problems, involving liquefaction of soil due to seismic effects. The incremental L_2 norm of error in strain for each solution step was used here in h-adaptive analysis, while linear 8-node hexahedral elements were used to discretise the problems' domains. The SPR method was extended to three-dimensional nonlinear problems, and its applications were explored in the transferring of the path dependent variables in [53, 54, 55]. Tetrahedral elements were used in the analysis, and different polynomials were used in the least squares fitting for the SPR method, possessing C_0, C_1 and C_2 continuity. In [56], an improvement of the SPR method, i.e. minimal patch recovery (MPR), was introduced in which there was no need to calculate the nodal stresses. The recovered solutions at Gauss points were calculated directly from the least squares projection of the Gauss points belong to the neighbouring elements. The method was applied to three-dimensional elasticity and metal forming problems with tetrahedral elements.

The same incremental procedure for the error estimation, used for the adaptive FEM in [28] and for the adaptive EFGM in [29] is used here, i.e. incremental global relative error in energy norm is calculated for each solution step, and checked against a permissible value. For solution step n, equations for the incremental error in energy norm and the corresponding energy norm for either an individual FE or EFG background cell Ω_e are given as

$$\|e_e^p\| = \left[\int_{\Omega_e} \left| \left(\boldsymbol{\tau}_n^p (\mathbf{x}) - \boldsymbol{\tau}_n^h (\mathbf{x}) \right)^T \left(\Delta \boldsymbol{\varepsilon}_n^p (\mathbf{x}) - \Delta \boldsymbol{\varepsilon}_n^h (\mathbf{x}) \right) \right| \mathrm{d}\Omega_e \right]^{\frac{1}{2}} \quad \text{and}$$

$$\|U_e\| = \left[\int_{\Omega_e} \left| \left(\boldsymbol{\tau}_n^p (\mathbf{x}) \right)^T \left(\Delta \boldsymbol{\varepsilon}_n^p (\mathbf{x}) \right) \right| \mathrm{d}\Omega_e \right]^{\frac{1}{2}}, \quad (37)$$

where the subscript e shows an individual FE or EFG background cell, $\boldsymbol{\tau}_n^p (\mathbf{x})$ and $\boldsymbol{\tau}_n^h (\mathbf{x})$ are the projected and numerical Kirchhoff stresses respectively at

a Gauss point $\mathbf{x}$ for solution step n, while $\Delta\boldsymbol{\varepsilon}_n^p(\mathbf{x})$ and $\Delta\boldsymbol{\varepsilon}_n^h(\mathbf{x})$ are the projected and numerical incremental logarithmic strains at a Gauss point $\mathbf{x}$ for the solution step n. Projected Kirchhoff stresses and the projected logarithmic strains in this case are calculated using the Zienkiewicz & Zhu and Chung & Belytschko procedures in the FE and the EFG region of the problem domain respectively. Equations for the error in energy norm and the corresponding energy norm for the problem domain Ω are then written as

$$\|e^p\|^2 = \sum_{i=1}^{n_{FE}} \|e^p_{FE}\|_i^2 + \sum_{j=1}^{n_{EFG}} \|e^p_{EFG}\|_j^2 \quad \text{and} \quad \|U\|^2 = \sum_{i=1}^{n_{FE}} \|U_{FE}\|_i^2 + \sum_{j=1}^{n_{EFG}} \|U_{EFG}\|_j^2 , \tag{38}$$

where n_{FE} and n_{EFG} are the total numbers of FEs and EFG background cells respectively in the problem domain. Incremental global relative percentage error and incremental permissible error in an individual FE or EFG background cell are written as

$$\eta = \frac{\|e^p\|}{\|U\|} \times 100 \qquad \text{and} \qquad \overline{\|e_e\|} = \frac{\overline{\eta}}{100} \left(\frac{\|U\|^2}{n} \right)^{\frac{1}{2}} , \tag{39}$$

where $n = n_{FE} + n_{EFG}$ and $\overline{\eta}$ is a permissible relative error for the whole problem domain.

5.1.1. Calculation of nodal stresses

The procedures to calculate nodal strains and stresses are now given separately for both FE and EFG region.

Finite element

For the FEM, the SPR method was developed by Zienkiewicz & Zhu [25] to calculate the nodal stresses and strains from the nodal displacements. In this procedure stresses and strains are initially calculated at the superconvergent points, which are then used to calculate stresses and strains at the nodes. It was shown that, in the cases of linear and cubic elements the recovered nodal stresses and strains are superconvergent (one order higher accurate or $O(h^{P+1})$), where h is the element size wheras ultraconvergence, i.e. $O(h^{P+2})$) or two orders higher accuracy was obtained in the case of quadratic elements.

The directly calculated nodal stresses and strains from the nodal displacements using the shape functions derivatives are however less accurate and discontinuous. Different strategies have been suggested in the literature to calculate accurate nodal stresses. One of the commonly used methods is averaging or local projection techniques, in which stresses are calculated at the nodes by extrapolation from the superconvergent sampling points, which are then averaged to get a single value. The accuracy of the stresses from this method is highly dependent on the existence of the superconvergent points in the FEs. Further detail and theoretical background of the superconvergent points within FEs and the averaging or local projection method can be found in, e.g. [57]. Other procedures for nodal stress recovery can also be found in the literature, including global projection [58] and extraction and other alternatives [59]. In all the above-mentioned nodal stress recovery methods, the nodal stresses obtained, are generally not superconvergent. In the SPR method, nodal stresses are calculated by using a discrete or local least square fitting over a set of superconvergent points in a patch of elements, assembled at a common node. The SPR method is superior to other stress recovery procedures because the recovered stresses are generally superconvergent or even ultraconvergent for the case of quadratic elements as stated above.

The objective of the SPR method is to find the nodal stresses $\boldsymbol{\sigma}_i^*$ such that a continuous and accurate stress field $\boldsymbol{\sigma}^*$ is obtained, i.e.

$$\boldsymbol{\sigma}^* = \sum_{i=1}^{n} N_i \boldsymbol{\sigma}_i^*, \tag{40}$$

where N_i is the same elemental shape function used in the displacement interpolation. Here the stress field $\boldsymbol{\sigma}^*$ is smooth throughout the problem domain and is more accurate than the corresponding directly calculated stress field $\boldsymbol{\sigma}^h$. In the SPR method, nodal stresses $\boldsymbol{\sigma}_i^*$ are obtained by the least squares fitting of the complete basis as used in the displacement approximation over a patch of elements surrounding an assembly node. The polynomial expansion of the stress component σ_p^* is written as

$$\sigma_p^* = \mathbf{P}\left(\mathbf{x}\right)\mathbf{a} \tag{41}$$

where $\mathbf{P}\left(\mathbf{x}\right)$ is the monomial basis function, $\mathbf{x}$ are spatial coordinates and $\mathbf{a}$ is a vector of unknown coefficients. For three-dimensional linear and quadratic

elements $\mathbf{P}(\mathbf{x})$ and corresponding $\mathbf{a}$ are

$$\mathbf{P}(\mathbf{x}) = \left\{ \begin{array}{cccc} 1, & x, & y, & z \end{array} \right\}, \qquad \mathbf{a} = \left\{ \begin{array}{ccc} a_1, & \cdots, & a_4 \end{array} \right\}^T, \tag{42a}$$

$$\mathbf{P}(\mathbf{x}) = \left\{ \begin{array}{cccccccccc} 1, & x, & y, & z, & xy, & yz, & zx, & x^2, & y^2, & z^2 \end{array} \right\}, \qquad \mathbf{a} = \left\{ \begin{array}{ccc} a_1, & \cdots, & a_{10} \end{array} \right\}^T. \tag{42b}$$

In (41), unknown coefficients $\mathbf{a}$ are determined separately for each patch by least squares fitting to the stresses at the superconvergent points. For the least squares fitting, the following equation is minimized w.r.t. $\mathbf{a}$

$$\mathbf{F}(\mathbf{a}) = \sum_{i=1}^{n} \left(\sigma^h(\mathbf{x}_i) - \sigma_p^*(\mathbf{x}_i) \right)^2 = \sum_{i=1}^{n} \left(\sigma^h(\mathbf{x}_i) - \mathbf{P}(\mathbf{x}_i)\,\mathbf{a} \right)^2, \tag{43}$$

where n is the total number of superconvergent points in a single patch of elements, $\mathbf{x}_i$ are the spatial coordinates of superconvergent points, $\sigma^h(\mathbf{x}_i)$ are the stresses calculated directly by the FEM at the superconvergent points and $\sigma_p^*(\mathbf{x}_i)$ are the recovered stresses at the same points using least square fitting. Minimization of (43) w.r.t. $\mathbf{a}$ gives

$$\mathbf{A}\mathbf{a} = \mathbf{b} \qquad \text{or} \qquad \mathbf{a} = \mathbf{A}^{-1}\mathbf{b}, \tag{44}$$

where

$$\mathbf{A} = \sum_{i=1}^{n} \mathbf{P}^T(\mathbf{x}_i)\,\mathbf{P}(\mathbf{x}_i) \qquad \text{and} \qquad \mathbf{b} = \sum_{i=1}^{n} \mathbf{P}^T(\mathbf{x}_i)\,\sigma^h(\mathbf{x}_i). \tag{45}$$

After calculating $\mathbf{a}$, nodal stresses are calculated from (41), i.e. using the nodal coordinates. The size of matrices $\mathbf{A}$ and $\mathbf{b}$ are very small and depend on $\mathbf{P}$. $\mathbf{b}$ should be determined separately for each stress component, while $\mathbf{A}^{-1}$ is the same for all stress components and is determined only once.

For the three-dimensional case, patches are shown in Figures 2(a) and 2(b) for 8-node and 20-node hexahedral elements respectively. In both patches, eight elements are joined at a common patch assembly node. In Figures 2(a) there is only one superconvergent point per element, and the patch is used to recover the stresses only at patch assembly nodes. In Figure 2(b) there are eight superconvergent points per element and patch are used to recover stresses at the patch assembly nodes as well as internal nodes, which are inside these patches, shown as solid circles. In Figure 2(b), internal nodes

normally belong to more than one patch, and stresses are recovered at these nodes from each patch, and the final stresses are then calculated by averaging. To recover stresses at boundary nodes, including essential/traction as well as interface between FE and EFG regions, internal or boundary patches can be used. Accuracy is the same, if stresses are recovered either from the boundary or internal patches [25]. In some situations, however, sufficient elements and superconvergent points are not available to construct patches at the boundary. Even if sufficient elements and superconvergent points are available, the construction of these boundary patches involves extra unnecessary work, as the stresses at boundary nodes can be recovered from the already constructed internal patches. To avoid these complications, in this paper internal patches are used to recover stresses at the boundary nodes.

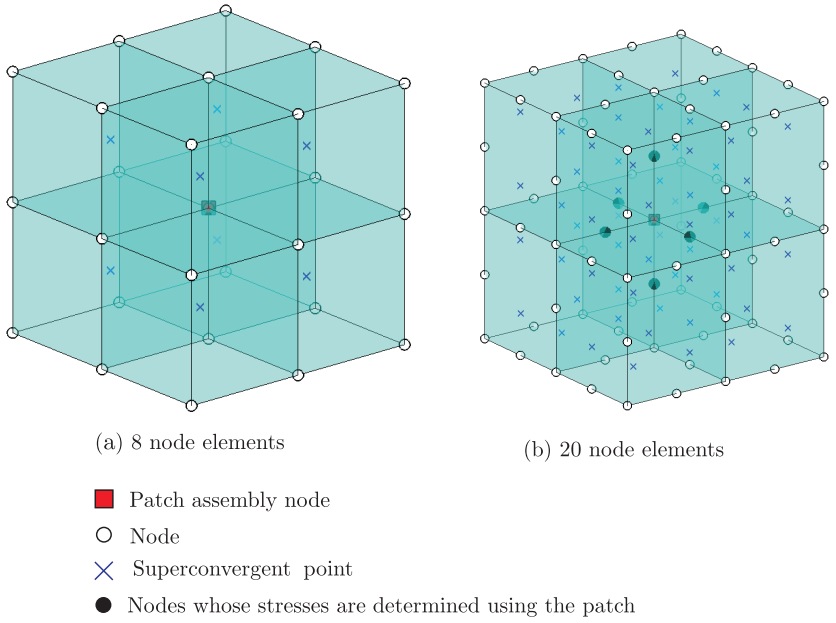

Figure 2: SPR three-dimensional elements patches

Element-free Galerkin method

As there are no elements in the EFGM, so there is no issue of strain and stress discontinuity, and the procedure used for the FEM is not directly applicable to the EFGM, because the derived stress and strain fields are

already smooth. The error estimation procedure proposed for the EFGM in [27] is used, in which projected stresses are calculated from the nodal stresses based on reduced domains of influence. It was also shown in [27] that the error estimator performs well when the domain of influence for stress projection is as small as possible but at the same time must be large enough to have sufficient nodes in support of each Gauss point required for the shape functions calculation. In the case of the EFGM, the stress and strain vector returned at any point $\mathbf{x}$ is written as

$$\boldsymbol{\sigma}^h(\mathbf{x}) = \sum_{i=1}^{n_a} \mathbf{D}\mathbf{B}_i\mathbf{u}_i \qquad \text{and} \qquad \boldsymbol{\varepsilon}^h(\mathbf{x}) = \sum_{i=1}^{n_a} \mathbf{B}_i\mathbf{u}_i, \tag{46}$$

where n_a is the number of nodes in the support of point $\mathbf{x}$ based on the domain of influence for analysis and $\mathbf{u}_i$ are fictitious nodal values for node i. The projected stress and strain vector at $\mathbf{x}$ are recovered from nodal stress and strain using

$$\boldsymbol{\sigma}^p(\mathbf{x}) = \sum_{j=1}^{n_p} \psi_j(\mathbf{x})\,\boldsymbol{\sigma}^h(\mathbf{x}_j) \qquad \text{and} \qquad \boldsymbol{\varepsilon}^p(\mathbf{x}) = \sum_{j=1}^{n_p} \psi_j(\mathbf{x})\,\boldsymbol{\varepsilon}^h(\mathbf{x}_j). \tag{47}$$

Here $\psi_j(\mathbf{x})$ is the shape function of a node j at a point $\mathbf{x}$ based on a reduced domain of influence and n_p is the number of nodes in the support of point $\mathbf{x}$ based on that reduced domain of influence and $\boldsymbol{\sigma}^h(\mathbf{x}_j)$ and $\boldsymbol{\varepsilon}^h(\mathbf{x}_j)$ are the nodal stresses and strains respectively.

5.2. Refinement strategy

The two-dimensional step-by-step refinement strategy (which is straightforward to modify for the three-dimensional case) used here is almost the same as used for the adaptive EFGM given in [60, 29] and is shown in Figure 3. The direct use of the adaptive EFGM refinement strategy here in the EFG region of the problem domain creates complications in the FE region of the problem domain, which requires further consideration. In this new strategy, refinement of the EFG background cells is the same as used in the original adaptive EFGM case, i.e. five new nodes are added in each background cell, which is then divided into four new cells. A sample coupled FE-EFGM discretisation is shown in Figure 3(a), in which columns A, B and C are the EFG background integration cells and columns D, E and F are FEs. The refinement of background cells in column A, B and C creates

hanging nodes in FEs, i.e. columns D in the FE region of the problem domain as shown in Figure 3(b). To avoid the complication of dealing with FEs with hanging nodes, the strategy used here is to convert all those FEs to the corresponding EFG background integration cells as shown in Figure 3(c). In the case of nonlinear problems due to the total Lagrangian formu-

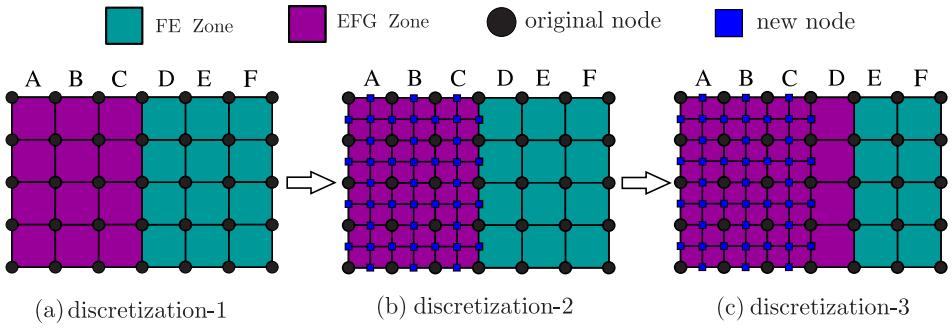

Figure 3: Step by step refinement strategy for the adaptive coupled FE-EFGM

lation, undeformed discretisations are refined as compared to the current or deformed discretisations refinements in the updated Lagrangian formulation. The same refinement strategy suggested originally for the two-dimensional linear elastic case, is also extended to three-dimensions. A major task in the nonlinear adaptive analysis is an accurate transfer of path dependent variables between the old and new discretisations. In this paper, the max-ent shape functions are used to transfer data from the old nodes and Gauss points to their new counterparts. The path dependent parameters for the nodes are displacement $\mathbf{u}$ and elastic logarithmic strain. For the Gauss points the variables are the same except for the omission of displacement. Writing any of these path dependent variables as ξ, transfer occurs using

$$\xi\left(\mathbf{x}_{new}\right) = \sum_{i=1}^{n_{old}} \psi_i\left(\mathbf{x}_{new}\right) \xi\left(\mathbf{x}_{old}\right)_i , \tag{48}$$

where $\mathbf{x}_{new}$ is the position of the new node or Gauss point, $\mathbf{x}_{old}$ is the position of old nodes or Gauss points, n_{old} is the number of old nodes or Gauss points in the support of $\mathbf{x}_{new}$ and $\psi_j\left(\mathbf{x}_{new}\right)$ are the max-ent shape functions.

5.3. Adaptive FE-EFGM coupling algorithm

The full adaptively coupled FE-EFGM algorithm for linear elastic problems is shown in Figure 4, which has been implemented in Matlab. At the

start of analysis, the whole of the problem domain is modelled with the FEM, which includes specification of geometry, material properties and meshing. Here four-node iso-parametric quadrilateral elements with (2×2) integration (or Gauss) points per element are used in the analysis. In this algorithm, itr is the current iteration and max itr is the maximum number of iterations specified by the user at the start of analysis. During each iteration, stiffness matrix is assembled, essential and traction boundary conditions are implemented and after solution of the final system of equations nodal displacements or fictitious nodal values are calculated for the FE and the EFG regions respectively. During the first iteration, nodal stresses are calculated using the standard SPR method and local and global relative errors are then calculated using the Zienkiewicz & Zhu error estimation procedure. This global relative error is then used to trigger the refinement algorithm, which converts FEs to EFG background cells.

From the second iteration onward, the problem domain consists of combined FE and EFG discretisations with (2×2) Gauss points per element in the FE region and (4×4) Gauss points in each background cell in the EFG region. After this point, error is only calculated for the EFG region, as FEs with high errors already converted into EFG background cells in the first iteration. After solution of the final system of equations, nodal stresses, local and global relative errors are calculated for the EFG region of the problem domain using the approach of Chung & Belytschko [27]. The global relative error is then used to decide further adaptive refinement in the EFG region, and those background cells, where error is more than the permissible error are automatically refined. As compared to the two-dimensional linear elastic counterpart, in which error in the FE region of the problem domain is calculated only in the first discretisation, in nonlinear case the error in the FE region of the problem domain is calculated during each evolving discretisation. Due to the incremental loading, it is expected in the subsequent discretisations that more elements will be converted to corresponding EFG background integration cells. The three-dimensional nonlinear adaptively coupled FE-EFGM algorithm has been implemented in FORTRAN90.

6. Numerical examples

Numerical examples are now given to demonstrate the correct implementation and performance of the full adaptively coupled FE-EFGM algorithm.

The first two numerical examples are linear elastic, while the last two are nonlinear.

6.1. Square block problem

The first numerical example is a plane stress square block subjected to uniform unit traction on the left edge and fully fixed on the bottom edge. The geometry, boundary conditions and loading for this problem are shown in Figure 5. The problem is solved with $E = 1 \times 10^3$, $\nu = 0.3$, $d^a_{max} = 1.5$, $d^p_{max} = 1.2$ and $\overline{\eta} = 6.0\,\%$, all in compatible units, where d^a_{max} and d^p_{max} are the scaling parameters for the domain of influence for analysis and projection respectively. The evolving step by step adaptively coupled FE-EFGM discretisations in this case are shown in Figure 6. The FE mesh at the start of analysis with $225\,(15 \times 15)$ elements and $256\,(16 \times 16)$ nodes is shown in Figure 6(a). The converted FEs to corresponding EFG background cells based on the Zienkiewicz & Zhu error estimation at the end of first iteration are shown in Figure 6(b). During this first FEs to EFG background cells conversion the number of nodes is constant. Subsequent refinements in the EFG regions of the problem domain, based on the Chung & Belytschko error estimation procedure, are shown in Figure 6(c). It can also be seen in Figure 6(c) that in the EFG zone on the right-hand side, all new nodes are added within the EFG region and there is no issue of hanging nodes in the FE region of the problem domain. However, in the EFG zone on the left-hand side, four more FEs at the top of EFG zone are converted to EFG background cells, to avoid hanging nodes in the FE region of the problem domain. As expected, the adaptively coupled FE-EFGM algorithm, initially converts the high-stress zones in the problem domain to the corresponding EFG zones and then adds nodes to the high-stress EFG zones. The contours of the von Misses stress over the problem domain after the first FE iteration are shown in Figure 7, which are obtained from the SPR method's recovered nodal stresses using the following equation

$$\sigma_{VM} = \left[\sigma^2_{xx} + \sigma^2_{yy} - \sigma_{xx}\sigma_{yy} + 3\sigma_{xy}\right]^{\frac{1}{2}}, \tag{49}$$

where σ_{xx} and σ_{yy} are the normal stresses in x and y directions and σ_{xy} is the shear stress. For comparison, the same problem is also solved with uniformly refined FE meshes with almost the same number of nodes as shown in Figures 6(a) and 6(c). The uniformly refined meshes in this case with $256\,(16 \times 16)$ and $400\,(20 \times 20)$ nodes are shown in Figures 8(a) and 8(b) respectively.

Comparison of the relative error (η) for the adaptively coupled FE-EFGM case and uniformly refined FEM case are shown in Figure 9, in which three data points are available for the adaptively coupled FE-EFGM case and only two data points are available in the uniformly refined FEM case. In Figure 9, it is clear that the decrease in the relative error is greater in the case of the adaptively coupled FE-EFGM as compared to the uniformly refined FEM case.

6.2. L-shaped plate

The second two-dimensional linear elastic numerical example is a plane stress L-shaped plate subjected to uniform pressure on the left edge, for which the geometry, boundary conditions and loading are shown in Figure 10 and is a standard numerical example to test the performances of adaptive algorithms. Here point A in Figure 10 is a point of high stress concentration due to the loading and boundary conditions. This problem is solved with $E = 1 \times 10^3$, $\nu = 0.25$, $d^a_{max} = 1.4$, $d^p_{max} = 1.1$ and $\overline{\eta} = 7.0\,\%$, all in compatible units. The step by step evolving discretisations in this case are shown in Figure 11. The FE mesh at the start of analysis with 341 nodes is shown in Figure 11(a) and the first and second adaptively coupled FE-EFGM discretisation with 341 and 406 nodes are shown in Figure 11(b) and 11(c) respectively. The number of nodes is the same in the first two discretisations. In 11(c) two more FEs are converted to the corresponding EFG background cells, to avoid hanging nodes in these elements. As expected, near the corner A in Figure 11, the adaptively coupled FE-EFGM algorithm converts the FE elements to EFG background cells and adds more nodes in the EFG region. The contours of von Mises stress after the first FE iteration over the problem geometry are also shown in Figure 12, which shows maximum stress near corner A. For comparison the same problem is also solved with the FEM with uniformly refined meshes with almost the same number of nodes as shown in Figure 11. The first and second uniformly refined meshes with 341 and 408 nodes are shown in Figure 13(a) and 13(b) respectively. Comparison between the relative error (η) for the adaptively coupled FE-EFGM case and uniformly refined FEM case is shown is Figure 14, in which the adaptively coupled FE-EFGM case clearly performs better than the uniformly refined FEM.

6.3. Three-dimensional plate with a hole

The first three-dimensional nonlinear numerical example is a plate with a central hole subjected to unidirectional tension; the same numerical example is also given in [61]. Geometry and loading for this problem are shown in Figure 15. Due to symmetry only the one-eighth of the problem shown in gray in Figure 15 is modelled with the material properties $E = 1.0 \times 10^5$, $\nu = 0.3$ and $\sigma_y = 1.0 \times 10^3$, all in compatible units. A total displacement of 0.15 units is applied to the top face in 15 equal steps. The scaling parameters used here for the domains of influence for analysis and projection in the EFG zone are $d^a_{max} = 1.5$ and $d^p_{max} = 1.1$ respectively and permissible relative error used is 25%. At the start of analysis, the whole of the problem domain is modelled using the FEM with 325 nodes as shown in Figure 16(a). For this first discretisation, the standard SPR method is used to recover the nodal stresses and incremental strains, which are then used in the Zienkiewicz & Zhu error estimation procedure. After first conversion, the second discretisation consists of both FEs and EFG background cells as shown in Figure 16(b), in which the number of nodes remains the same. From the second discretisation onward, both Zienkiewicz & Zhu and Chung & Belytschko error estimation procedures are used in the FE and the EFG regions of the problem domain respectively. Subsequent discretisations after further conversion of the FEs to the EFG background cells and refinement in the EFG background cells are shown in Figures 16(c) and 16(d). The number of nodes in the third and fourth discretisations are 929 and 4119 respectively. The adaptively coupled FE-EFGM algorithm based on the combined Zienkiewicz & Zhu and Chung & Belytschko error estimation procedures add nodes automatically in the thinning section of the plate as expected.

The contours of the displacements u_x and u_y are shown in Figures 17(a) and 17(b) respectively, in which as expected the total deformation is concentrated next to the hole. The contours of the effective plastic strain are also shown in Figure 17(c), in which a shear band of finite thickness next to the hole is clearly evident. Reaction versus displacement plot for this problem is given in Figure 18. For comparison, the same problem is also solved without adaptivity, using different initial FE and coupled FE-EFGM discretisations shown in Figure 16 for which the reaction versus displacement plots are shown in Figure 18 for comparison. In this case, the solution obtained with final adaptively coupled FE-EFGM discretisation shown in Figure 16(d) is considered as a reference. As compared to the coupled FE-EFGM cases, the FEM response is relatively rigid without obvious geometric softening behaviour.

The convergence of the reaction versus displacement curves to the reference solution, with an increasing the number of nodes can also be observed in Figure 18, which shows the correct implementation and effectiveness of the proposed adaptively coupled FE-EFGM algorithm.

6.4. Three-dimensional footing loaded on a vertical cut

The second three-dimensional nonlinear numerical example solved by the proposed approach is a three-dimensional footing loaded near the unsupported faces of a vertical cut. The geometry and loading for this problem are shown in Figure 19(a). This problem was solved with material properties $E = 2.0 \times 10^4$, $\nu = 0.3$ and $\sigma_y = 30$ all in compatible units. Here only the soil section of the problem is modelled with the adaptively coupled FE-EFGM with total vertical displacement of 0.1 units applied to nodes beneath the footing in 15 equal steps. The scaling parameters used here for the domains of influence for analysis and projection in the EFG zone are $d^a_{max} = 1.5$ and $d^p_{max} = 1.1$ respectively and permissible relative error used is 25%. The FE mesh at the start of the analysis is shown in Figure 19(b) and the step by step conversion of the FEs to the EFG background cells and subsequent refinements of the EFG background cells are shown in Figures 19(c), 19(d) and 19(e). The number of nodes used in first two discretisations is 729, while in the subsequent discretisations, the number of nodes increases to 1215 and 2950. For this problem, failure is expected in the soil below the footing, where FEs are automatically converted to the EFG background cells, which are refined in the subsequent discretisations. The contours of u_y and effective plastic strain are also shown in Figures 20(a) and 20(b) respectively. It can be seen in Figure 20(a), that the total displacement is concentrated below the footing and a very clear shear band of finite thickness can also be seen in Figure 20(b). A reaction versus displacement plot for this problem is shown in Figure 21. For comparison, the same problem is also solved with different starting discretisations shown in Figure 19 without adaptivity and plots for the reaction versus displacement are shown also in Figure 21. The solution with discretisation 19(e) is considered as a reference solution in this case. Convergence of the adaptively coupled FE-EFGM case and all other cases to the reference solution is clear in Figure 21. It is obvious from the plot that the adaptive solution has a number of jumps in the curve. The jumps represent points where rediscretisation is taking place and mapping has been carried out. These changes are due to recalculation of the equilibrium state of the domain due to the altered discretisation. They should not be con-

fused with jumps in displacements. These plots show results from successive analysis not a single calculation.

7. Concluding remarks

In this paper, a new numerical method is developed for solid mechanics in which initially, the whole of the problem domain is modelled using the FEM and during the analysis adaptive refinement changes FE regions to EFG regions. Two established error estimation procedures have been adapted for use here, one for FEs and the other for the EFGM regions. Refinement of the created EFG regions is also included. The full implementation and performance of the linear elastic adaptively coupled FE-EFGM algorithm is demonstrated with the help of two two-dimensional numerical examples. Results are also compared with the FEM uniform refinement case, and it is shown that the proposed method performs better in terms of decrease in the relative error. The adaptively coupled FE-EFGM algorithm is also extended to challenging three-dimensional cases with both material and geometrical nonlinearities. Total Lagrangian formulations are used instead of updated Lagrangian formulations to model finite deformation due to computational efficiency. Incremental forms of the Zienkiewicz & Zhu error estimation procedure and the Chung & Belytschko's error estimation procedures are used in this case in the FE and EFG region of the problem domain. The implementation and performance of the nonlinear adaptively coupled FE-EFGM algorithm is also demonstrated with two three-dimensional numerical examples.

Acknowledgements

The first author was supported by an Overseas Research Students Awards Scheme award from Durham University during the research which led to this paper.

References

[1] T. Belytschko, Y. Y. Lu, L. Gu, Element-free Galerkin methods, International Journal for Numerical Methods in Engineering 37 (1994) 229–256.

[2] T. Rabczuk, T. Belytschko, Cracking particles: a simplified meshfree method for arbitrary evolving cracks, International Journal for Numerical Methods in Engineering 61(13) (2004) 2316–2343.

[3] T. Rabczuk, G. Zi, A meshfree method based on the local partition of unity for cohesive cracks, Computational Mechanics 39(6) (2007) 743–760.

[4] T. Rabczuk, T. Belytschko, A three dimensional large deformation meshfree method for arbitrary evolving cracks, Computer Methods in Applied Mechanics and Engineering 196(29-30) (2007) 2777–2799.

[5] T. Rabczuk, S. Bordas, G. Zi, A three-dimensional meshfree method for continuous multiplecrack initiation, nucleation and propagation in statics and dynamics,, Computational Mechanics 40(3) (2007) 473–495.

[6] S. Bordas, T. Rabczuk, G. Zi, Three-dimensional crack initiation, propagation, branching and junction in non-linear materials by extrinsic discontinuous enrichment of meshfree methods without asymptotic enrichment, Engineering Fracture Mechanics 75(5) (2008) 943–960.

[7] T. Rabczuk, G. Zi, S. Bordas, H. Nguyen-Xuan, A geometrically nonlinear three dimensional cohesive crack method for reinforced concrete structures, Engineering Fracture Mechanics 75(16) (2008) 4740–4758.

[8] T. Rabczuk, J. Eibl, L. Stempniewski, Simulation of high velocity concrete fragmentation using SPH/MLSPH, International Journal for Numerical Methods in Engineering 56(10) (2003) 1421–1444.

[9] X. Zhuang, C. E. Augarde, S. P. Bordas, Accurate fracture modelling using meshless methods, the visibility criterion and level sets: Formulation and 2D modelling, International Journal for Numerical Methods in Engineering 86 (2) (2011) 249–268.

[10] X. Zhuang, C. E. Augarde, K. M. Mathisen, Fracture modeling using meshless methods and level sets in 3D: Framework and modeling, International Journal for Numerical Methods in Engineering 92 (2012) 969–998.

[11] X. Zhuang, C. E. Heaney, C. E. Augarde, On error control in the element-free Galerkin method, Engineering Analysis with Boundary Elements 36 (3) (2012) 351 – 360.

[12] X. Zhuang, C. E. Augarde, Aspects of the use of orthogonal basis functions in the element-free Galerkin method, International Journal for Numerical Methods in Engineering 81 (3) (2010) 366–380.

[13] T. Belytschko, D. Organ, Y. Krongauz, A coupled finite element-element-free Galerkin method, Computational Mechanics 17 (1995) 186–195.

[14] S. Fernández-Méndez, A. Huerta, Enrichment and coupling of the finite element and meshless methods, International Journal for Numerical Methods in Engineering 48 (2000) 1615–1636.

[15] A. Huerta, S. Fernández-Méndez, W. K. Liu, A comparison of two formulations to blend finite elements and mesh-free methods, Computer Methods in Applied Mechanics and Engineering 193 (2004) 1105 – 1117.

[16] D. Hegen, Element-free Galerkin methods in combination with finite element approaches, Computer Methods in Applied Mechanics and Engineering 135 (1-2) (1996) 143 – 166.

[17] T. Rabczuk, T. Belytschko, Application of particle methods to static fracture of reinforced concrete structures, International Journal of Fracture 137 (2006) 19–49.

[18] Y. T. Gu, L. C. Zhang, Coupling of the meshfree and finite element methods for determination of the crack tip fields, Engineering Fracture Mechanics 75 (5) (2008) 986 – 1004.

[19] Q. Xiao, M. Dhanasekar, Coupling of FE and EFG using collocation approach, Advances in Engineering Software 33 (2002) 507 – 515.

[20] T. Rabczuk, S. P. Xiao, M. Sauer, Coupling of mesh-free methods with finite elements: basic concepts and test results, Communications in Numerical Methods in Engineering 22 (10) (2006) 1031–1065.

[21] Z. Ullah, C. Augarde, W. Coombs, Local maximum entropy shape functions based FE-EFGM coupling, submitted to International Journal for Numerical Methods in Engineering.

[22] H. Karutz, R. Chudoba, W. Krätzig, Automatic adaptive generation of a coupled finite element/element-free Galerkin discretization, Finite Elements in Analysis and Design 38 (11) (2002) 1075 – 1091.

[23] L. Liu, X. Dong, C. Li, Adaptive finite element-element-free Galerkin coupling method for bulk metal forming processes, Journal of Zhejiang University - Science A 10 (2009) 353–360.

[24] O. C. Zienkiewicz, J. Z. Zhu, A simple error estimator and adaptive procedure for practical engineerng analysis, International Journal for Numerical Methods in Engineering 24 (1987) 337–357.

[25] O. C. Zienkiewicz, J. Z. Zhu, The superconvergent patch recovery and a posteriori error estimates. Part 1: The recovery technique, International Journal for Numerical Methods in Engineering 33 (7) (1992) 1331–1364.

[26] O. C. Zienkiewicz, J. Z. Zhu, The superconvergent patch recovery and a posteriori error estimates. Part 2: Error estimates and adaptivity, International Journal for Numerical Methods in Engineering 33 (7) (1992) 1365–1382.

[27] H.-J. Chung, T. Belytschko, An error estimate in the EFG method, Computational Mechanics 21 (1998) 91–100.

[28] B. Boroomand, O. Zienkiewicz, Recovery procedures in error estimation and adaptivity. Part II: Adaptivity in nonlinear problems of elasto-plasticity behaviour, Computer Methods in Applied Mechanics and Engineering 176 (1-4) (1999) 127 – 146.

[29] Z. Ullah, C. Augarde, Finite deformation elasto-plastic modelling using an adaptive meshless method, Computers & Structures 118 (2013) 39–52.

[30] C. E. Shannon, A mathematical theory of communication, The Bell Systems Technical Journal 27 (1948) 379–423.

[31] A. I. Khinchin, Mathematical foundation of information theory, Dover Publications, Inc. , New York, 1957.

[32] E. T. Jaynes, Information theory and statistical mechanics, Physical Review 106 (1957) 620–630.

[33] E. T. Jaynes, Information theory and statistical mechanics-II, Physical Review 108 (1957) 171–190.

[34] N. Sukumar, Construction of polygonal interpolants: a maximum entropy approach, International Journal for Numerical Methods in Engineering 61 (2004) 2159–2181.

[35] M. Arroyo, M. Ortiz, Local *maximum-entropy* approximation schemes: a seamless bridge between finite elements and meshfree methods, International Journal for Numerical Methods in Engineering 65 (2006) 2167–2202.

[36] N. Sukumar, R. W. Wright, Overview and construction of meshfree basis functions: from moving least squares to entropy approximants, International Journal for Numerical Methods in Engineering 70 (2007) 181–205.

[37] C. J. Cyron, M. Arroyo, M. Ortiz, Smooth, second order, non-negative meshfree approximants selected by maximum entropy, International Journal for Numerical Methods in Engineering 79 (13) (2009) 1605–1632.

[38] D. González, E. Cueto, M. Doblaré, A higher order method based on local maximum entropy approximation, International Journal for Numerical Methods in Engineering 83 (6) (2010) 741–764.

[39] A. Rosolen, D. Mill e n, M. Arroyo, On the optimum support size in meshfree methods: A variational adaptivity approach with maximum-entropy approximants, International Journal for Numerical Methods in Engineering 82 (7) (2010) 868–895.

[40] N. Sukumar, Fortran 90 Library for *Maximum-Entropy Basis Functions*. User's Reference Manual Version 1.4. Code available at http://www.imechanica.org/node/3424 (2008).

[41] B. Nayroles, G. Touzot, P. Villon, Generalizing the finite element method: Diffuse approximation and diffuse elements, Computational Mechanics 10 (1992) 307–318.

[42] W. Ji, A. M. Waas, Z. P. Bazant, Errors caused by non-work-conjugate stress and strain measures and necessary corrections in finite element programs, Journal of Applied Mechanics 77 (4) (2010) 044504 (1–5).

[43] W. M. Coombs, R. S. Crouch, C. E. Augarde, 70-line 3D finite deformation elastoplastic finite-element code, in: Proc. Numerical Methods in Geotechnical Engineering (NUMGE), Trondheim, Norway, June 3-5 2010, pp. 151–156.

[44] B. BOROOMAND, O. C. ZIENKIEWICZ, Recovery by equilibrium in patches (REP), International Journal for Numerical Methods in Engineering 40 (1) (1997) 137–164.

[45] Y. Hu, M. F. Randolph, H-adaptive FE analysis of elasto-plastic non-homogeneous soil with large deformation, Computers and Geotechnics 23 (1-2) (1998) 61 – 83.

[46] M. Kitanmra, H. Gu, H. Nobukawa, A study of applying the superconvergent patch recovery (SPR) method to large deformation problem, Journal of the Society of Naval Architects of Japan (187) (2000) 201–208.

[47] H. Gu, Z. Zong, K. Hung, A modified superconvergent patch recovery method and its application to large deformation problems, Finite Elements in Analysis and Design 40 (2004) 665 – 687.

[48] I. Babuška, T. Strouboulis, C. S. Upadhyay, S. K. Gangaraj, K. Copps, Validation of a posteriori error estimators by numerical approach, International Journal for Numerical Methods in Engineering 37 (7) (1994) 1073–1123.

[49] M. Ainsworth, J. T. Oden, A Posteriori Error Estimation in Finite Element Analysis, John Wiley & Sons, NewYork, 2000.

[50] C. K. Choi, N. H. Lee, A 3D adaptive mesh refinement using variable-node solid transition elements, International Journal for Numerical Methods in Engineering 39 (9) (1996) 1585–1606.

[51] H. Moslemi, A. Khoei, 3D adaptive finite element modeling of non-planar curved crack growth using the weighted superconvergent patch

recovery method, Engineering Fracture Mechanics 76 (11) (2009) 1703 – 1728.

[52] T. Xiaowei, S. Tadanobu, Adaptive mesh refinement and error estimate for 3-D seismic analysis of liquefiable soil considering large deformation, Journal of natural disaster science 26 (1) (2004) 37–48.

[53] A. Khoei, S. Gharehbaghi, The superconvergence patch recovery technique and data transfer operators in 3D plasticity problems, Finite Elements in Analysis and Design 43 (8) (2007) 630 – 648.

[54] S. Gharehbaghi, A. Khoei, Three-dimensional superconvergent patch recovery method and its application to data transferring in small-strain plasticity, Computational Mechanics 41 (2008) 293–312.

[55] A. Khoei, S. Gharehbaghi, Three-dimensional data transfer operators in large plasticity deformations using modified-SPR technique, Applied Mathematical Modelling 33 (7) (2009) 3269 – 3285.

[56] R. Boussetta, L. Fourment, A posteriori error estimation and three-dimensional adaptive remeshing: Application to error control of non-steady metal forming simulations, AIP Conference Proceedings 712 (1) (2004) 2246–2251.

[57] O. Zienkiewicz, R. Taylor, The Finite Element Method Set, Elsevier Science, 2005.

[58] O. C. Zienkiewicz, X. K. Li, S. Nakazawa, Iterative solution of mixed problems and the stress recovery procedures, Communications in Applied Numerical Methods 1 (1) (1985) 3–9.

[59] I. Babuška, A. M. ., The post-processing approach in the finite element method — Part I: Calculation of displacements, stresses and other higher derivatives of the displacements, International Journal for Numerical Methods in Engineering 20 (6) (1984) 1085–1109.

[60] T. Rabczuk, T. Belytschko, Adaptivity for structured meshfree particle methods in 2D and 3D, International Journal for Numerical Methods in Engineering 63 (11) (2005) 1559–1582.

[61] Y. T. Feng, D. Perić, Coarse mesh evolution strategies in the Galerkin multigrid method with adaptive remeshing for geometrically non-linear problems, International Journal for Numerical Methods in Engineering 49 (4) (2000) 547–571.

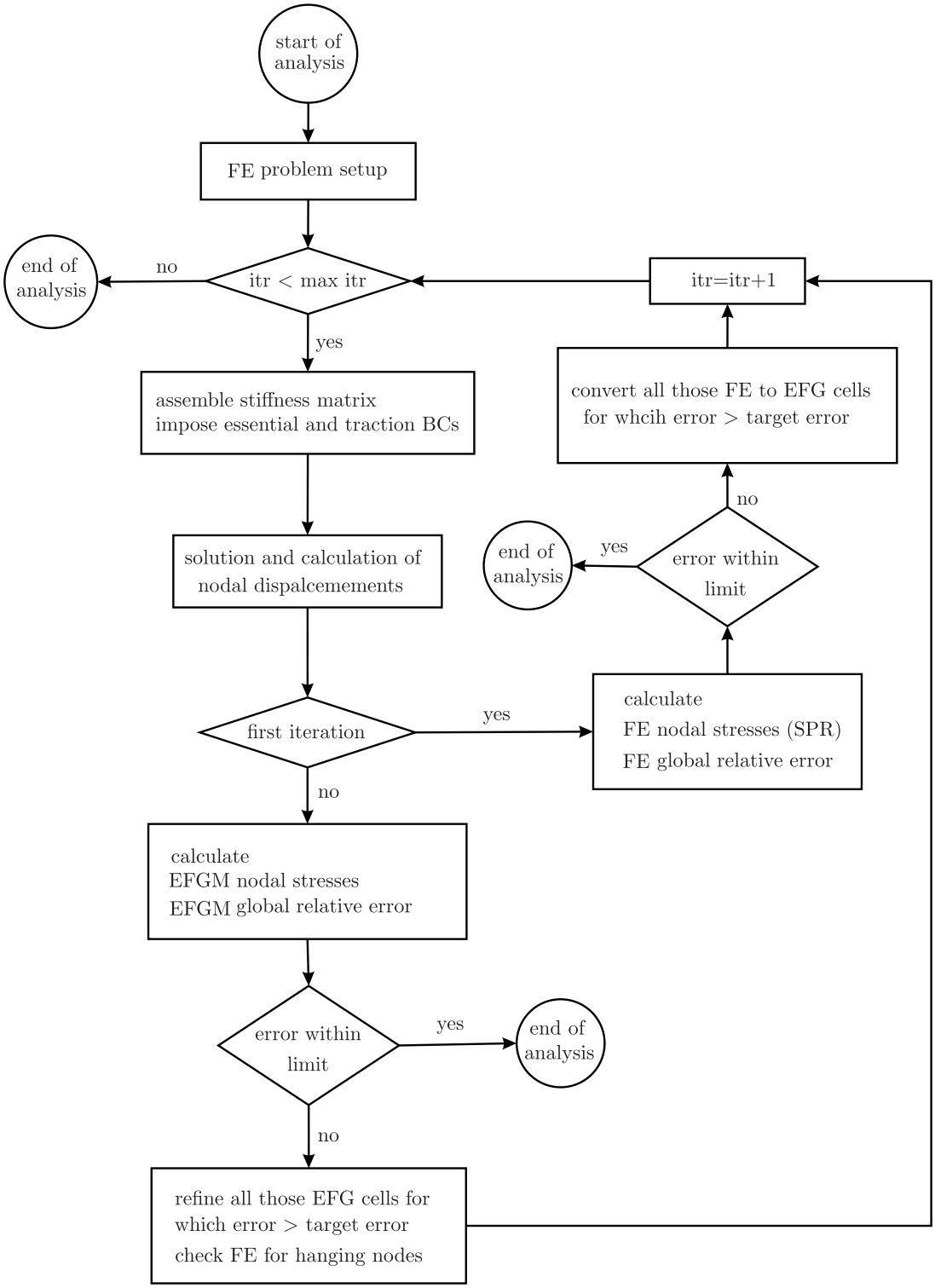

Figure 4: Adaptively coupled FE-EFGM algorithm for linear elastic problems

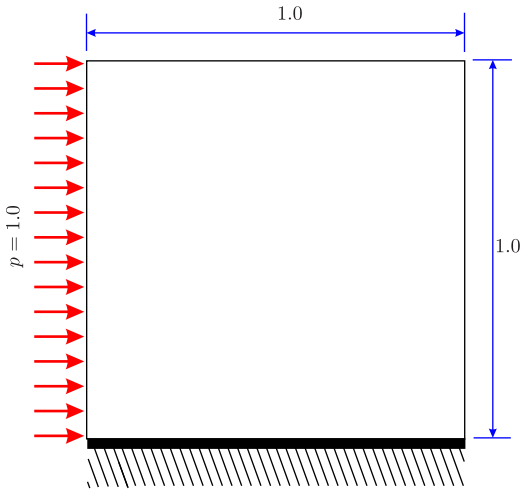

Figure 5: Geometry, boundary condition and loading for the square block problem

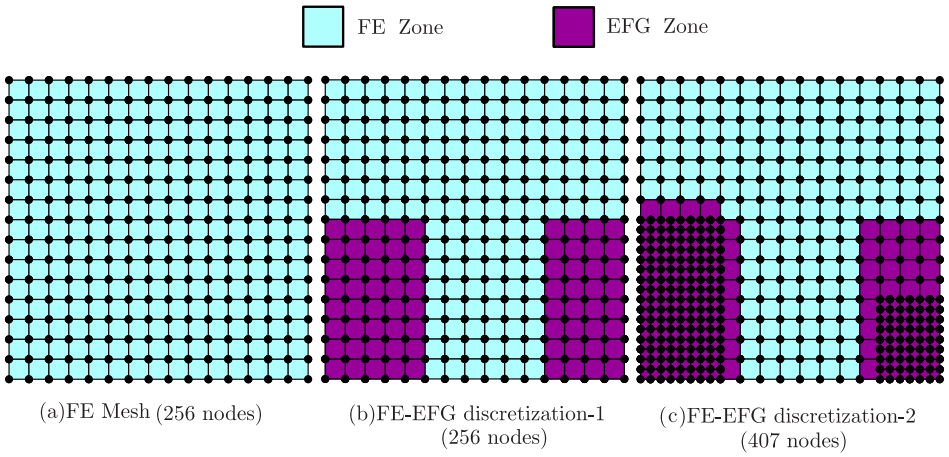

Figure 6: Step by step discretisations for the square block problem

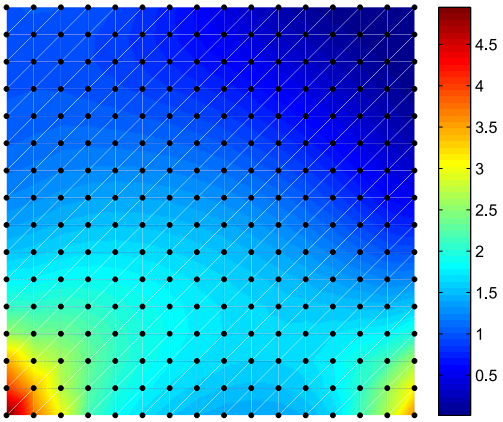

Figure 7: Von Misses stress contours for the square block problem

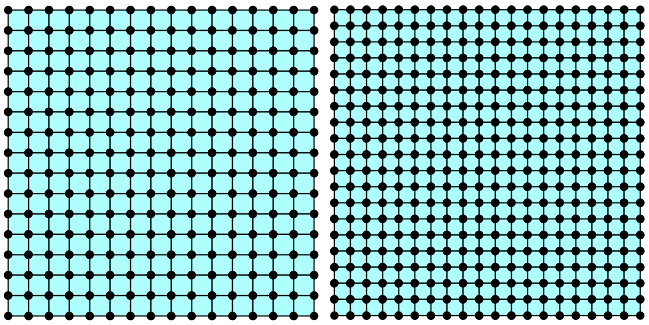

(a) FE mesh-1 (256 nodes) (b) FE mesh-2 (400 nodes)

Figure 8: Step by step FE uniform refinement for the square block problem

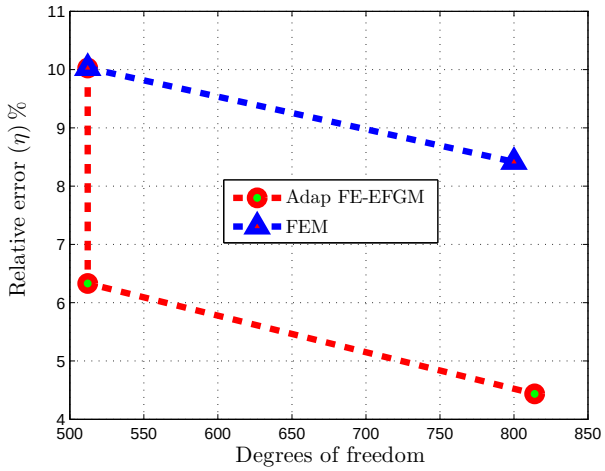

Figure 9: Relative error $(\eta)\,\%$ for the square block problem

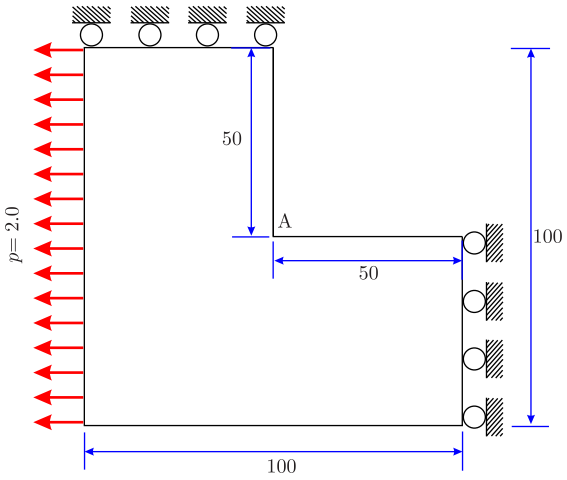

Figure 10: Geometry, boundary condition and loading for the L-shaped plate problem

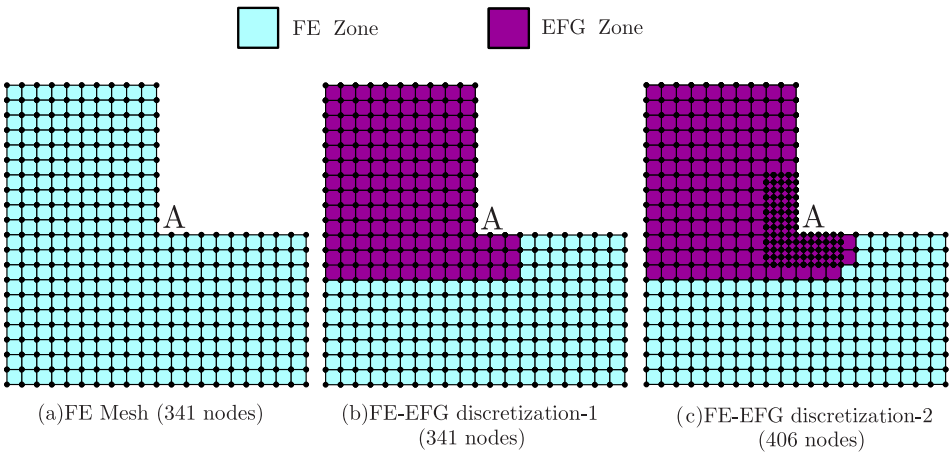

Figure 11: Step by step discretisations for the L-shaped plate problem

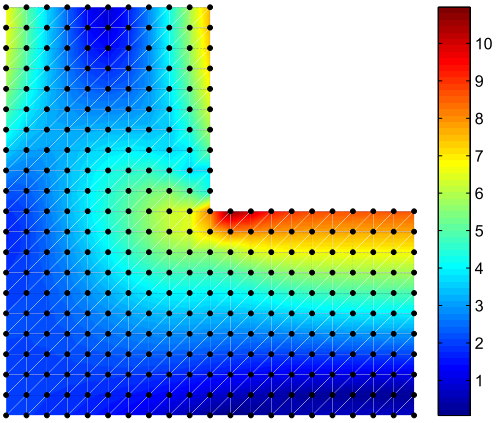

Figure 12: Von Misses stress contours for the L-shaped plate problem

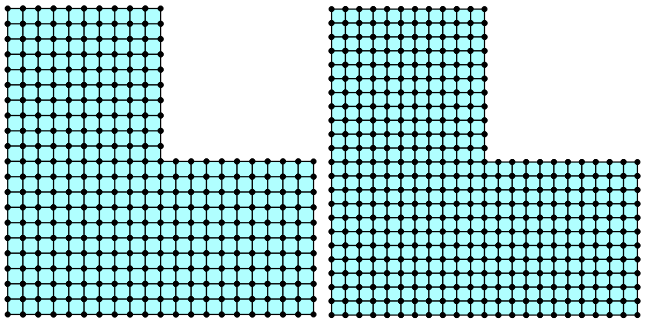

(a) FE mesh-1 (341 nodes) (b) FE mesh-2 (408 nodes)

Figure 13: Step by step FE uniform refinement for the L-shaped plate problem

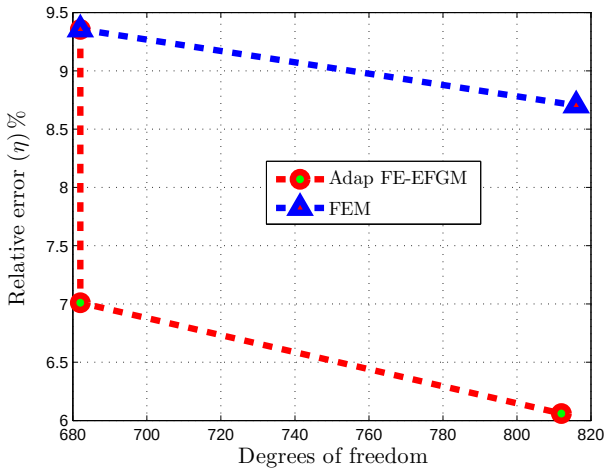

Figure 14: Relative error $(\eta)\,\%$ for the L-shaped plate problem

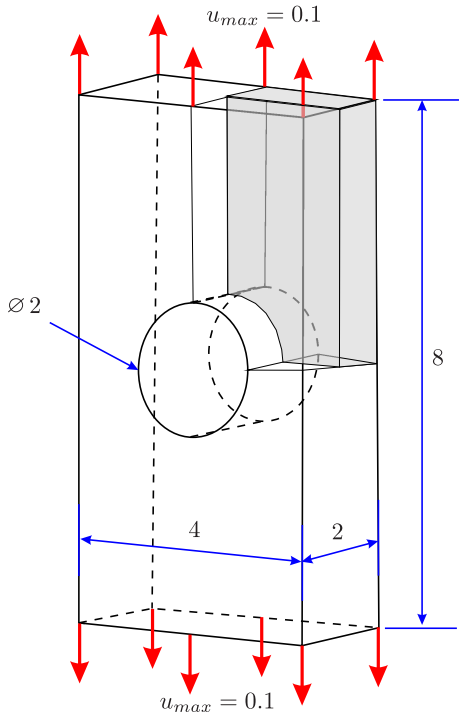

Figure 15: Geometry, boundary condition and loading for the 3D plate with a hole problem

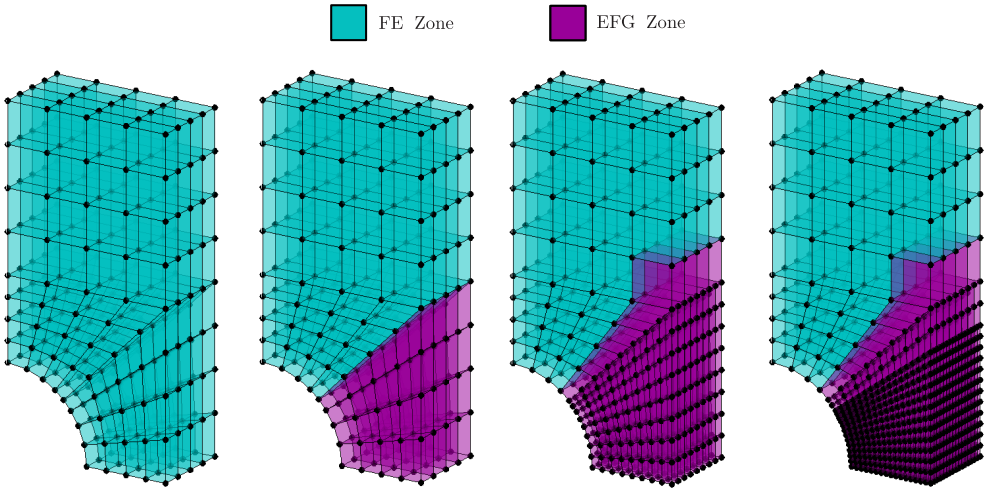

(a) FE mesh (325 nodes)

(b) FE-EFG discretizaiton-1 (325 nodes)

(c) FE-EFG discretizaiton-2 (929 nodes)

(d) FE-EFG discretizaiton-3 (4119 nodes)

Figure 16: Step by step discretisations for the three-dimensional plate with a hole problem

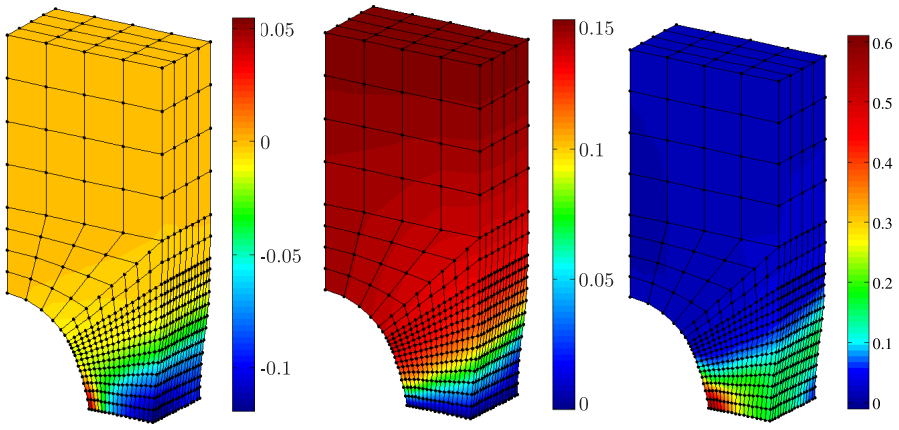

(a) u_x contours (b) u_y contours (c) effective plastic strain

Figure 17: Displacements and effective plastic strain contours for the three-dimensional plate with a hole problem

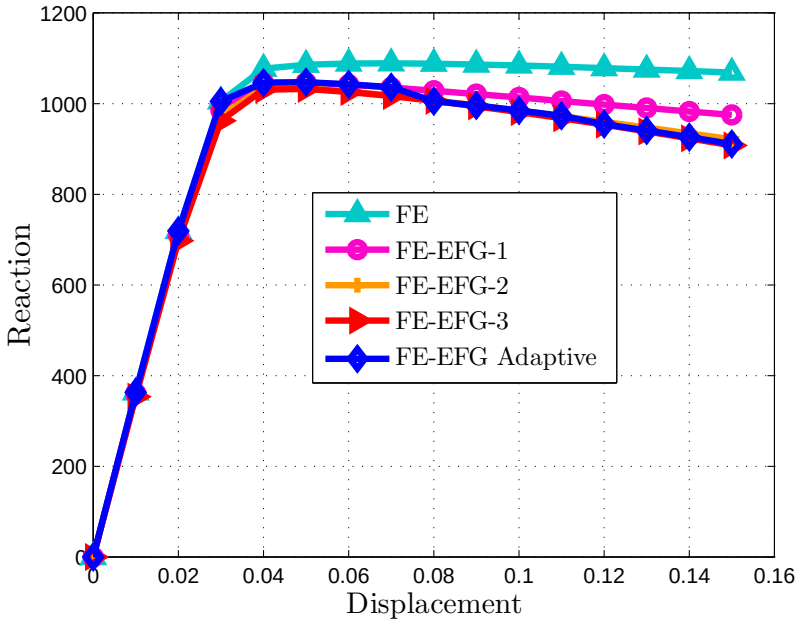

Figure 18: Reaction versus displacement for the three-dimensional plate with a hole problem

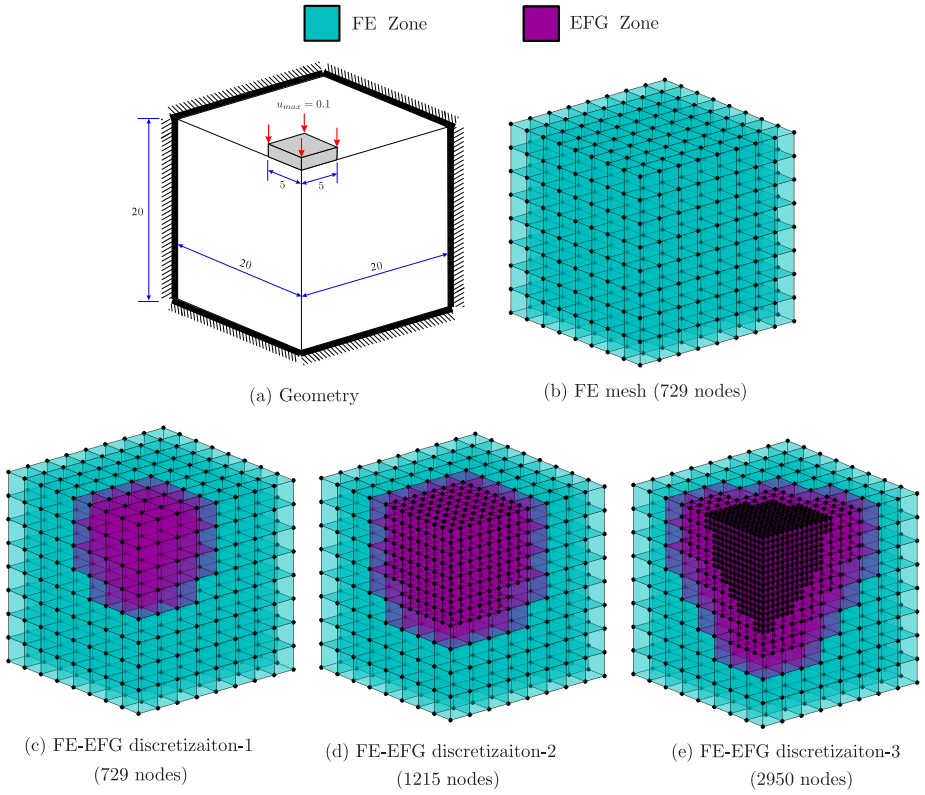

Figure 19: Step by step discretisations for the three-dimensional vertical cut problem problem

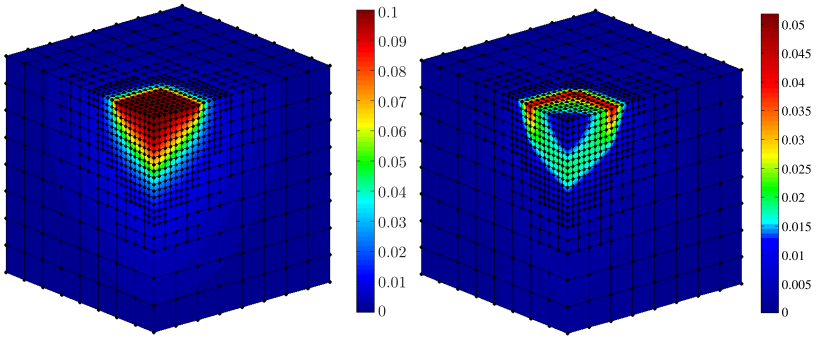

Figure 20: Displacement u_y and effective plastic strain contours for the three-dimensional vertical cut problem

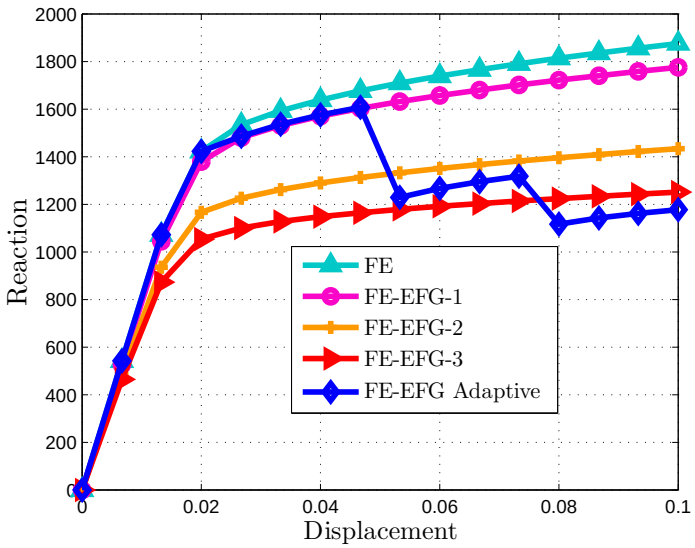

Figure 21: Reaction versus displacement for the three-dimensional vertical cut problem